Journal of Alloys and Compounds 565 (2013) 127–133

Contents lists available at SciVerse ScienceDirect

Journal of Alloys and Compounds

journal homepage: www.elsevier.com/locate/jalcom

Mechanical properties of Cr-alloyed $MoSi_2$-based nanocomposite coatings with a hierarchical structure

Jiang Xu [a,*], Jia di Wu [a], Zhengyang Li [b], Paul Munroe [c], Zong-Han Xie [d]

[a] Department of Material Science and Engineering, Nanjing University of Aeronautics and Astronautics, 29 Yudao Street, Nanjing 210016, PR China
[b] Institute of Mechanics, Chinese Academy of Sciences, Beijing 100190, PR China
[c] School of Materials Science and Engineering, University of New South Wales, Sydney, NSW 2052, Australia
[d] School of Mechanical Engineering, University of Adelaide, SA 5005, Australia

ARTICLE INFO

Article history:
Received 29 October 2012
Received in revised form 19 February 2013
Accepted 20 February 2013
Available online 6 March 2013

Keywords:
Transition metal silicides
First-principle calculation
Nanocomposite
Mechanical properties
Residual stresses

ABSTRACT

Novel Cr-alloyed $MoSi_2$-based nanocomposite coatings were successfully synthesized onto Ti–6Al–4V substrates by a double glow discharge plasma technique. The architecture of the nanocomposite coatings exhibited a hierarchical structure, consisting of equiaxed C40-$MoSi_2$ with a bimodal grain size distribution and strip-shaped Mo_5Si_3 grains segregated to the boundaries of submicron $MoSi_2$ grains. The results showed that the toughness of the $MoSi_2$-based nanocomposite coatings depended strongly upon their hierarchical structure and the magnitude of compressive residual stresses in the nanocomposite coatings.

1. Introduction

Owing to its unique combination of a high melting point, superior high-temperature stability and strength, and excellent oxidation resistance at high temperatures, molybdenum disilicide ($MoSi_2$) has received much attention as a promising coating material for structural application in extremely harsh environments [1]. However, monolithic $MoSi_2$ suffers some severe deficiencies, such as poor low ambient temperature toughness and pest oxidation at moderate temperatures, which restrict its application as a protective coating [2,3]. Much effort has been devoted to overcoming these problems through substitutional alloying or forming nanocomposites [4–6]. For example, Cr additions can mitigate pest oxidation of $MoSi_2$ due to Cr having a strong affinity to oxygen [7,8]. $MoSi_2$ is a dimorph compound, which possess a hexagonal close-packed C40 structure with a $P6_222$ space group between the melting point and 1900 °C and a tetragonal body-centered $C11_b$ structure with a I4/mmm space group below this temperature [9,10]. In comparison with the well investigated $C11_b$ structured $MoSi_2$, little work has addressed the issue of the mechanical behavior of C40 structured $MoSi_2$, which is mainly attributed to the difficulty in fabricating metastable C40-structured $MoSi_2$ through conventional processing methods. Theoretical calculations have revealed that the reduction of symmetry from $C11_b$ structured to C40 structured $MoSi_2$ can lead to an improvement in ductility [11]. Therefore, it is imperative to explore different strategies to toughen monolithic C40 structured $MoSi_2$.

In this study, the influence of Cr additions on the lattice constants and mechanical parameters (bulk modulus, shear modulus, Young's modulus, and Poisson's ratio) of C40 structured $MoSi_2$ were explored by first-principles calculations based on density functional theory. Furthermore, $MoSi_2$-based nanocomposite coatings with varying Cr contents were deposited on Ti–6Al–4V substrates by a double glow discharge plasma technique. The effects of microstructural feature, Cr contents and compressive residual stresses on the mechanical properties of $MoSi_2$-based nanocomposite coatings were investigated.

2. Experimental method and computational details

Four Cr-alloyed $MoSi_2$-based nanocomposite coatings were deposited on mirror-polished Ti–6Al–4V alloy substrates by a double cathode glow discharge technique using four targets with different stoichiometric ratios ($Mo_{25}Si_{75}$, $Mo_{25}Cr_3Si_{72}$, $Mo_{23}Cr_5Si_{72}$ and $Mo_{20}Cr_8Si_{72}$), respectively. Inside the chamber, one cathode is used as the target and the other as the substrate, as described elsewhere [12]. The glow discharge sputtering conditions were as follows: base pressure, 4×10^{-4} Pa; target electrode bias voltage, −900 to −950 V; substrate bias voltage, −300 to −350 V; working pressure, 35 Pa; parallel distance between the source electrode and the substrate, 15 mm and treatment time of 3 h. The sputtering targets were fabricated from ball-milled Mo (99.99% purity), Cr (99.99% purity) and Si powders (99.99% purity) by employing cold compaction under a pressure of 600 MPa. Sub-

* Corresponding author.
E-mail address: xujiang73@nuaa.edu.cn (J. Xu).

0925-8388/$ - see front matter © 2013 Elsevier B.V. All rights reserved.
http://dx.doi.org/10.1016/j.jallcom.2013.02.134

strate materials used were Ti–6Al–4V alloy with a diameter of 40 mm and a thickness of 3 mm. Before sputter deposition, the substrates were polished using silicon carbide abrasive paper of 2400 grit and then ultrasonically cleaned in pure alcohol and water. For the sake of brevity, the coatings prepared using $Mo_{25}Si_{75}$, $Mo_{25}Cr_3Si_{72}$, $Mo_{23}Cr_5Si_{72}$ and $Mo_{20}Cr_8Si_{72}$ targets are referred to as M1(deposition temperature, 800 °C) and M2–4 (deposition temperature, 900 °C), respectively.

The phase compositions of the as-deposited coatings were studied using a X-ray diffractometer (XRD, D8ADVANCE with Cu Kα radiation) operating at 35 kV and 40 mA. X-ray data were collected using a 0.1° step scan with a counting time of 1 s. The as-deposited coatings were etched in Kroll's reagent (10 mL HNO_3, 4 mL HF and 86 mL distilled water) for 20–30 s. The microstructure and chemical composition of the as-deposited coatings were examined by scanning electron microscopy (SEM, Quanta 200, FEI Company) incorporating X-ray energy dispersive spectroscopy (EDS, EDAX Inc.) and transmission electron microscopy (TEM, Tecnai G220, FEI Company). Plan-view TEM samples were prepared using a single-jet electro-chemical polishing technique from the untreated side of the substrate. Nanoindentation tests were conducted on all the as-deposited coatings using a nanoindentation tester (an Ultra-Micro Indentation System (UMIS) 2000). Subsurface sectioning and imaging of indentation sites corresponding to a maximum load of 500 mN were carried out using a dual electron/focused ion beam (FIB) system (Nova Nanolab 200, FEI Company, Hillsboro, OR 97124, USA).

First-principles calculations were performed based on the plane-wave pseudopotential within the density functional theory (DFT) using the Cambridge Serial Total Energy Package (CASTEP) [13–15]. The interactions between ionic core and valence electrons were defined by the ultrasoft pseudo-potentials and the valence electrons considered for Mo, Cr and Si, were $4s^24p^64d^55s^1$, $3s^23p^63d^54s^1$ and $3s^23p^2$, respectively. The exchange–correlation energy was described by the generalized gradient approximation (GGA) with the Perdew–Burke–Ernzerhoh (PBE) [16] functional. Brillouin zone sampling was carried out using a $6 \times 6 \times 4$ set of Monkhorst–Pack *k*-points mesh and a plane-wave cutoff energy of 350 eV was employed in the calculations [17].

To generate compositions close to experimental stoichiometries, $2 \times 2 \times 1$ supercells consisting of 36 atoms were constructed for C40-structured $(Mo_{1-x}Cr_x)Si_2$ where Mo atoms were replaced by 1–3 Cr atoms and the corresponding Cr concentrations (i.e., '*x*' value) were 0.083, 0.167 and 0.250, respectively. Geometry optimizations were first performed to obtain equilibrium structures using Broyden–Fletcher–Goldfarb–Shanno minimization (BFGS) methods [18]. Both lattice parameters and atomic coordinates were relaxed until the total energy tolerance was smaller than 5.0×10^{-6} eV/atom, the maximum ionic Hellmann–Feynman force within 0.01 eV/Å, the maximum ionic displacement within 5.0×10^{-4} Å, and the maximum stress within 0.02 GPa.

3. Results and discussion

The mechanical parameters for C40-structured $(Mo_{1-x}Cr_x)Si_2$, including bulk modulus (*B*), shear modulus (*G*), Young's modulus (*E*), G/B ratio and Poisson's ratio (*v*), can be extracted from the calculated elastic constants by the Voigt–Reuss–Hill (VRH) approach [19]. The calculated mechanical parameters for C40-structured $(Mo_{1-x}Cr_x)Si_2$ are plotted in Fig. 1. Our calculated values for bulk modulus and shear modulus for binary C40 $MoSi_2$ differ from the theoretical values obtained by other investigations by only 3% and 1.6%, respectively, demonstrating the reliability of our present calculations [11]. As shown in Fig. 1a, with increasing Cr concentration, the bulk modulus, shear modulus and Young's modulus slightly increase. These quantities are of fundamental importance for understanding the mechanical behavior of materials. Since hardness depends mainly on plastic deformation associated with the creation and motion of dislocations, shear modulus exhibits a linear correlation with the hardness of materials [20,21]. As a result, Cr alloying may increase the hardness of C40-structured $MoSi_2$, resulting in solid solution hardening. Moreover, brittleness or ductility of a material is closely related to the elastic properties of a crystal. For instance, Pugh [22] proposed the ratio of bulk to shear modulus G/B, as a key parameter to distinguish brittle and ductile behaviors for a solid at a critical value of 0.57, where below this value the material behaves in a ductile manner; otherwise, the material behaves in a brittle manner. As shown in Fig. 1b, it is clear that C40-structured $(Mo_{1-x}Cr_x)Si_2$ can be classified as a brittle material based on the Pugh criteria, and the calculated G/B values for C40-structured $(Mo_{1-x}Cr_x)Si_2$ are essentially independent of Cr content. Poisson's ratio, *v*, provides more information about the characteristics of the bonding forces compared with other elastic constants [23]. It is generally assumed that the smaller Poisson's ratio, the stronger the directionality of atomic bonding. Our calculated values for Poisson's ratio are larger than that reported for $C11_b$-structured $MoSi_2$ and C40-structured $CrSi_2$, denoting that the directionality in atomic bonding in C40-structured $(Mo_{1-x}Cr_x)Si_2$ is weaker [24]. On the other hand, Poisson's ratio, characterizes the stability of the crystal against shearing strain, and is widely used as a useful criterion for brittleness [25]. Obviously, the variation of the Poisson's ratios for C40-structured $(Mo_{1-x}Cr_x)Si_2$ with Cr additions is similar to that for the G/B ratio.

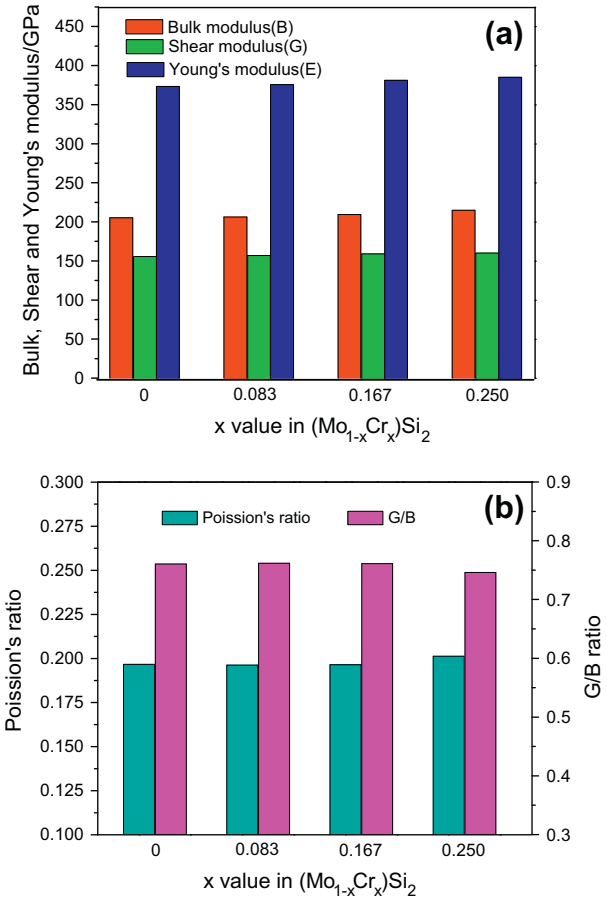

Fig. 1. The Calculated mechanical parameters for C40 structured $(Mo_{1-x}Cr_x)Si_2$: (a) Bulk, shear and Young's modulus; (b) Poisson's ratio and G/B ratio.

As shown in Fig. 2a, X-ray diffraction data reveal that the M1 coating consists of monolithic C40-structured $MoSi_2$ with a pronounced (1 1 1) orientation texture, whereas the M2–4 coatings are composed mostly of C40-structured $MoSi_2$ with minor concentrations of D8m-structured Mo_5Si_3. It should be noted, however, that C40-$MoSi_2$ can form as a metastable intermediate phase either during the phase transformation from amorphous to $C11_b$-$MoSi_2$ or during thin film deposition [26,27]. Similar to other PVD processes, the coatings grown by glow discharge deposition often exist in a non-equilibrium state, characterized by limited atomic assembly kinetics. Under such conditions, the mechanism of phase formation in the coatings is governed by the nucleation model, suggesting that the phase with either the fastest nucleation rate or the lowest nucleation barrier is the most likely to be formed. Because the activation energy for the formation of C40-$MoSi_2$ (1.5 eV) is smaller than that for $C11_b$-$MoSi_2$ (7.8 eV), the nucleation of the C40-$MoSi_2$ phase needs to overcome a lower energy barrier and, thus, can readily be formed during glow discharge deposition [27]. Moreover, the positions of $MoSi_2$ diffraction peaks for the four coatings shift to lower 2θ values with reference to the powder diffraction

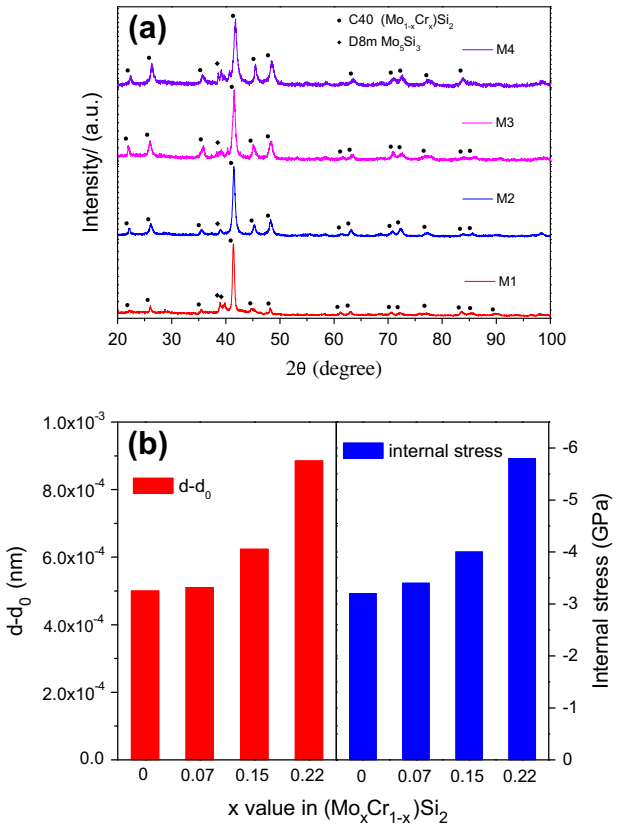

Fig. 2. (a) XRD patterns of the M1–M4 coatings; (b) the red histogram represents the difference between d and d_0 versus x value, while the blue one represents the variation of compressive residual stresses with x value. (For interpretation of the references to color in this figure legend, the reader is referred to the web version of this article.)

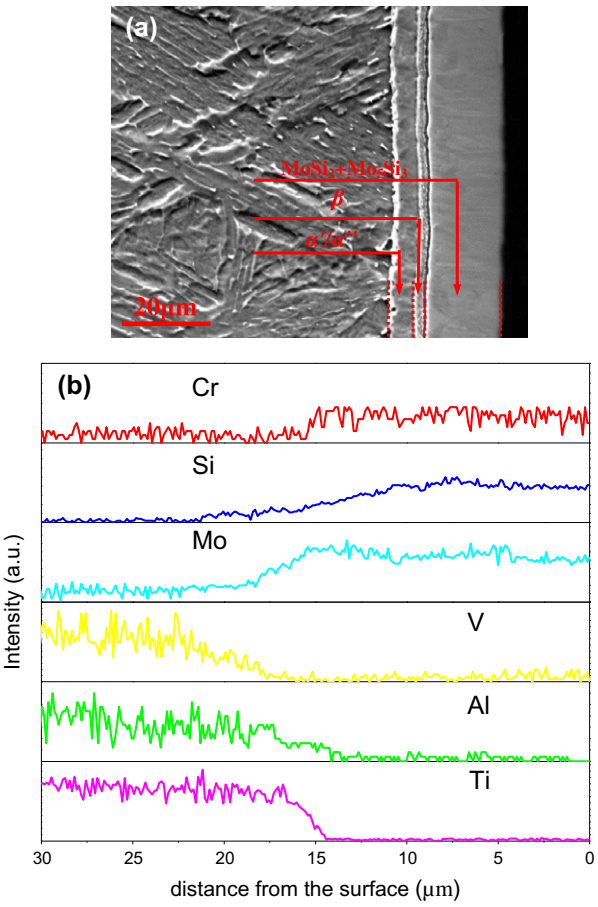

Fig. 3. (a) Cross-section SEM images of M2 coating; (b) The elemental concentration profiles across the entire thickness of the M2 coating measured by an EDS line scan.

standard. This is due to both Cr atoms being present in solid solution in the $MoSi_2$ phase and the presence of residual stresses in the coatings. After deduction of the contribution of composition-dependence to the observed d-spacings for $MoSi_2$, a rough estimation of the residual stresses in the coatings can be determined via the expression [28]:

$$\sigma = -\frac{E}{\nu}\left(\frac{d_n - d_0}{d_0}\right) \quad (1)$$

where E, ν, d_n and d_0 are, respectively, the Young's modulus, Poisson's ratio, d-spacing of the (1 1 1) plane obtained from the experiment and calculated d-spacing of the (1 1 1) plane as a strain-free reference. The results show that the four coatings exhibit significant compressive residual stresses in the range of 3.2–5.8 GPa, and that the residual compressive stresses increase with Cr content (Fig. 2b). The presence of residual stresses in the coatings is attributable to differences in the mechanical and thermal properties between the substrate and coatings and/or different phases in the coatings [29]. As shown in Fig. 3a, the as-deposited coatings exhibit a dense and homogeneous microstructure without any visible defects, and are securely anchored to the substrates. By a combination of the XRD results and EDS analysis (Fig. 3b), the microstructure of the four as-deposited coatings consists of an outer silicide layer and an inner Mo diffusion layer. The ~15 μm thick outer layer is composed of monolithic C40-structured $MoSi_2$ (M1) or $MoSi_2 + Mo_5Si_3$ (M2–4), and the ~6 μm thick inner Mo diffusion layer is generated by Mo atoms diffusing from the outer layer into the substrate, which results in the phase transformations of $\beta \rightarrow \alpha'' \rightarrow \alpha'$, as described in our previous paper [12]. Fig. 4a and b shows representative plan-view TEM micrographs taken from the outer layers of the M1 and M2 coatings. For the M1 coating, $MoSi_2$ grains exhibit an equiaxed morphology with an average grain size of about 5 nm, confirmed later by the high resolution TEM image (inset in Fig. 4a). In contrast, through selected-area electron diffraction (SAED) analyses, the M2 coating (Fig. 4b) consists mainly of $MoSi_2$ with small amounts of Mo_5Si_3. In this composite coating, the $MoSi_2$ grains exhibit a bimodal grain size distribution, consisting of fine grains with an average grain size of 5 nm and coarser grains with an average grain size of ~250 nm due to the growth of fine-grained $MoSi_2$ at the higher deposition temperature, while the strip-shaped Mo_5Si_3 grains segregate to the grain boundaries of the coarse-grained $MoSi_2$. Moreover, it can be seen from Fig. 4c that some dislocations are distributed within the coarse-grained $MoSi_2$. Quantitative analysis of phase composition by EDS (Fig. 4d and e) indicates that no appreciable change in composition between the coarse-grained and fine-grained $MoSi_2$ phase can be observed, and their compositions in the M1–4 coatings can be identified as $(Mo_{1-x}Cr_x)Si_2$ (x = 0, 0.07, 0.15 and 0.22), respectively; whereas the Mo_5Si_3 phase contains higher Cr contents than the $MoSi_2$ phase, implying that the formation of Mo_5Si_3 phase may stem from Cr segregation to $MoSi_2$ grain boundaries. A similar finding was also observed by StrÖm et al. [7], who found that Cr-containing Mo_5Si_3 phases are located along the grain boundaries of $MoSi_2$ grains in samples prepared by sintering of powders with specific compositions ($(Mo_{0.90}Cr_{0.10})Si_2$ and $(Mo_{0.85}Cr_{0.15})Si_2$). Thus, with increasing Cr content, the fraction of Cr-rich Mo_5Si_3 phases increases, leading

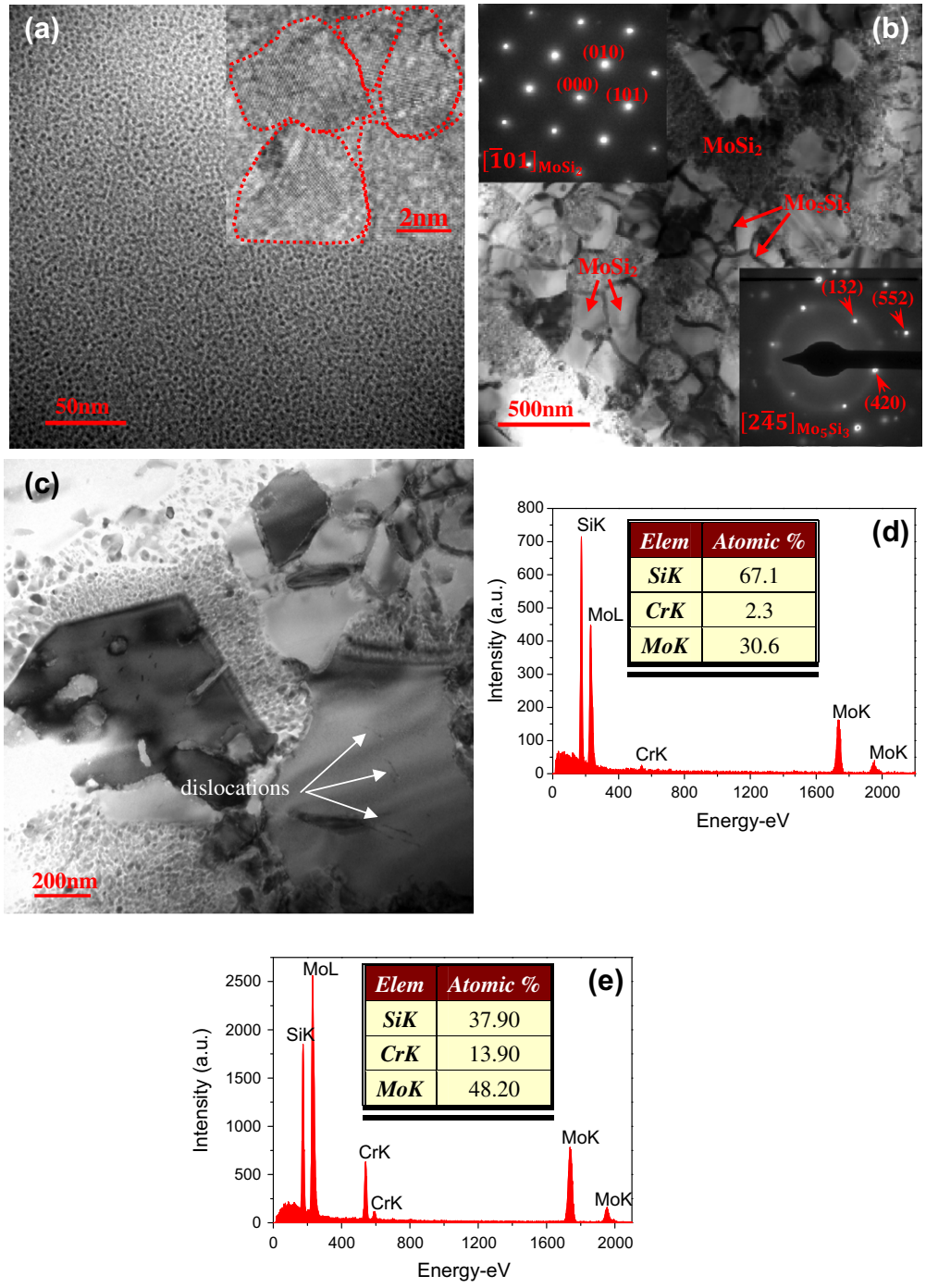

Fig. 4. (a) A typical plan-view bright-field TEM image of the M1 coating and the corresponding high-resolution lattice image (right upper inset); (b) A typical plan-view bright-field TEM image of the M2 coating. Two insets in (b) are the corresponding SAED patterns of $MoSi_2$ and Mo_5Si_3 phases. (c) Bright field TEM images showing dislocations (marked by arrows) in the "coarser" $(Mo_{1-x}Cr_x)Si_2$ grains. EDS area analysis from the $MoSi_2$ (d) and Mo_5Si_3 phases(e) in the M2 coating.

to the presence of a higher compressive residual stress in the as-deposited coatings.

Fig. 5a shows the representative load–displacement (P–h) curves for the M1–4 coatings under a maximum load of 20 mN and the measured hardness values are plotted in the inset of Fig. 5a. Note that the maximum indentation depth is less than 10% of the coating thickness, indicating that the contribution to the measured mechanical properties from the substrate is likely to be negligible. The hardness values of the coatings increase with increasing Cr content, which are in accord with the calculated results for shear modulus. Moreover, the compressive stresses within the coatings also enhance indented hardness, and thus the coatings with a higher Cr content have a higher hardness [30]. Fig. 5b shows SEM micrographs of representative indentation impressions on the coatings under an indentation load of 1 kg and a dwell time of 15 s. Except for the M4 coating, no evidence of cracks formation or propagation at the corners of the indentation impressions could be observed for the M1–3 coatings. According to the formula used to estimate fracture toughness [31], the calculated indentation fracture toughness value for the M4 coating is about 11.5 MPa $m^{1/2}$, which is 2.6 times higher than that of a $MoSi_2$–SiC nanocomposite with an average grain size of 60 nm

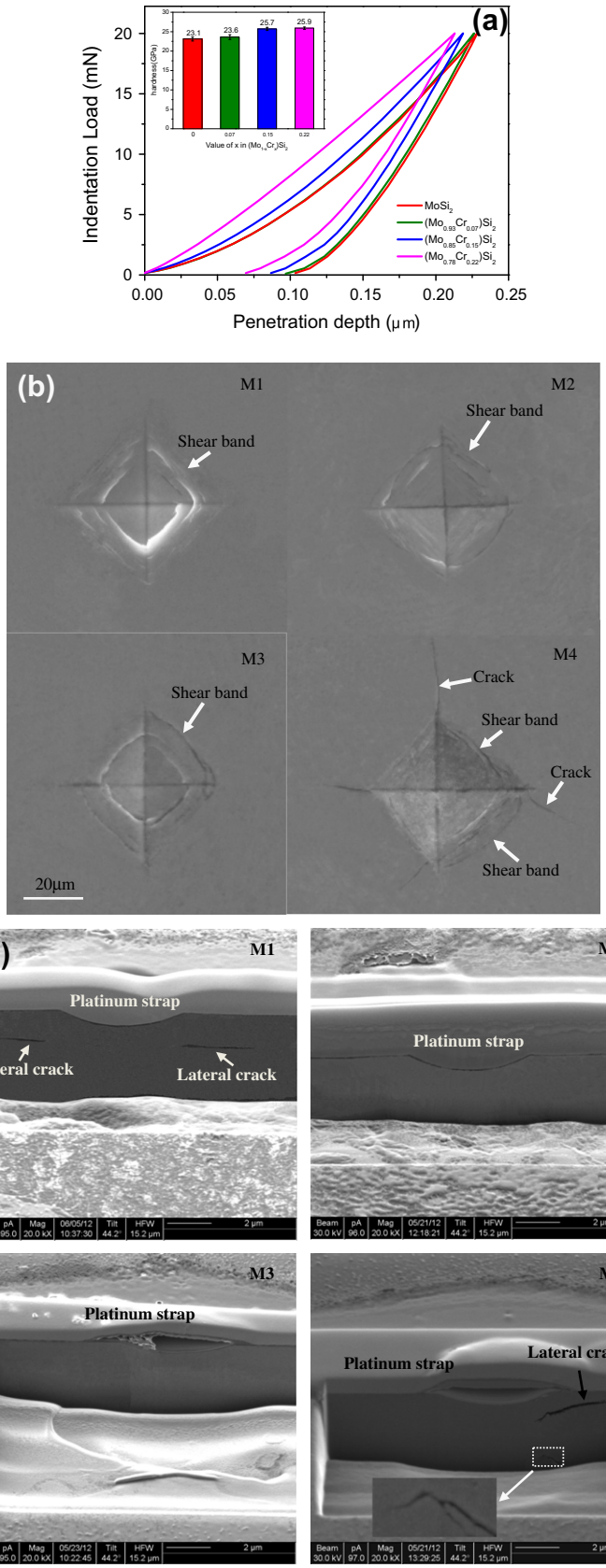

Fig. 5. (a) Load–displacement curves of the M1–4 coatings. The inset in (a) shows the measured hardness values of the M1–4 coatings. (b) SEM micrographs of representative Vickers indentations on the M1–4 coatings under a load of 1000 g. (c) Secondary electron FIB images showing cross-sections of the M1–4 coatings subjected to nanoindentation to 500 mN using a 5 μm radius indenter.

(4.3 MPa $m^{1/2}$) [6]. Remarkably, some annular shear band patterns were observed within the Vickers indentations, which is a feature often found in indentation impressions in metallic glasses [32]. Based on the above observations, it is reasonable to deduce that the primary deformation mode in these coatings is accommodated by shear band formation and propagation, which is analogous to that of bulk metallic glasses. To further explore contact damage beneath the indentations, cross-sections through the indentations on the coatings were prepared by focused ion beam (FIB) milling. Fig. 5c presents FIB cross-sectional images of indents on the four coatings, subjected to loads of 500 mN using a 5 μm radius spherical-tipped indenter. Lateral cracks within the sub-surface are observed to propagate parallel to surface of the M1 coating. For the M4 coating, one lateral crack initiated at the contact edge due to the severe shear stresses existing in this region, running outside of the indent area; the other is visible at a deeper depth propagating downward, which may be attributed to crack propagation perpendicular to the highest principal stress direction in the underlying elastoplastic region [33]. Further, the crack path in the M4 coating is more tortuous than that of the M1coating, indicating that the existence of a potential crack deflection mechanism in the M4 coating that would increase the required energy for crack propagation. However, no crack is detectable within the cross-sections taken from the M2 and M3 coatings under identical loading conditions, reflecting that the toughness of the two coatings is higher than that of the M1and M4 coatings.

As mentioned above, Cr additions have no effect on the toughness of $(Mo_{1-x}Cr_x)Si_2$, and thus, the main reasons for the significant variation of mechanical properties among the four coating must arise from microstructural features and residual stresses within the four coatings. Recent experiment observations and molecular dynamics simulations have indicated that grain boundary sliding or grain boundary rotation is the primary deformation mechanism in nanocrystalline materials with grain sizes <50 nm [34–36]. Therefore, the M1 coating with an average grain size of 5 nm, has to rely on the grain boundary activity to accommodate the plastic deformation. However, numerous investigations on nanocrystalline materials indicated that a grain boundary-mediated plasticity is insufficient, compared to that for a dislocation-mediated plasticity, which results in absence of adequate strain hardening to resist plastic flow instabilities, such as necking and shear banding [37–39]. On the contrary, for the M2–4 nanocomposite coatings which exhibit a bimodal microstructure, the deformation of these grains is under a complex stress state with very large strain gradients [40]. During plastic deformation, submicron-scale $(Mo_{1-x}Cr_x)Si_2$ grains which exhibit dislocation activity, accommodate strains preferentially, and subsequently local stress concentrations transfer to the surrounding fine-grained $(Mo_{1-x}Cr_x)Si_2$,when yielding occurs initially within the coarse-grained $(Mo_{1-x}Cr_x)Si_2$ [41]. Unlike the M1 coating, the coarse $(Mo_{1-x}Cr_x)Si_2$ grains act as obstacles which restrict the propagation of shear bands in the fine-grained $(Mo_{1-x}Cr_x)Si_2$, and such obstructive action imposed by the coarse $(Mo_{1-x}Cr_x)Si_2$ grains alters the direction of shear sliding and thus promotes the formation of multiple shear-bands [42]. Consequently, a marked improvement in toughness for the M2–3 coatings originates from accumulations of dislocations in the "coarser" $(Mo_{1-x}Cr_x)Si_2$ grains and the interaction between the shear bands inside the fine-grained $(Mo_{1-x}Cr_x)Si_2$ and the coarse $(Mo_{1-x}Cr_x)Si_2$ grains, which enhances work-hardening capacity. Further, the residual stress caused by presence of Mo_5Si_3 at the grain boundaries may facilitate crack deflection and bifurcation, also improving fracture toughness [5]. On the other hand, the role of the residual stress within the coatings on fracture toughness should be also noted. Generally, suitable compressive residual stresses within the coatings are beneficial since they inhibit crack initiation and propagation to some degree. Holmberg et al. [43] investigated the effect of compressive residual stresses, for PVD deposited TiN and DLC coatings, on fracture toughness. They found that compressive residual stresses in these coatings are in the range of 0.5–4 GPa, and these higher compressive residual stresses result in higher fracture toughness. These results are consistent with experimental observation for the M1–3 coatings. Nevertheless, it seems that the higher compressive stress in the M4 coating seems to be deleterious to toughness, because extremely high stresses can lead to delamination and intra-coating fracture [44].

4. Conclusions

In this study, the influence of Cr alloying on the mechanical properties of $MoSi_2$ with a C40 structure was explored by first principles calculations. The calculated results show that alloying with Cr has no effect on the toughness of C40 structured $(Mo_{1-x}Cr_x)Si_2$. Furthermore, novel Cr-alloyed $MoSi_2$-based nanocomposite coatings with a hierarchical structure were deposited on Ti–6Al–4V substrates by a double glow discharge plasma technique. The results showed that the toughness of the Cr-alloyed $MoSi_2$-based nanocomposite coatings is strongly dependent upon their hierarchical structure and the magnitude of compressive residual stresses in the nanocomposite coatings.

Acknowledgement

The authors acknowledge the financial support of the National Natural Science Foundation of China under Grant No. 51175245.

References

[1] M. Zakeri, R. Yazdani-Rad, M.H. Enayati, M.R. Rahimipour, J. Alloys Comp. 403 (2005) 258–261.
[2] J.J. Petrovic, Intermetallics 8 (2000) 1175–1182.
[3] U.V. Waghmare, V. Bulatov, E. Kaxiras, M.S. Duesbery, Mater. Sci. Eng. A 261 (1999) 147–157.
[4] W. Soboyejo, D. Brooks, L.C. Chen, J. Am. Ceram. Soc. 78 (1995) 1481–1488.
[5] K. Niihara, Y. Suzuki, Mater. Sci. Eng. A 261 (1999) 6–15.
[6] M. Patel, J. Subramanyuam, V.V. Bhanu Prasad, Scripta Mater. 58 (2008) 211–214.
[7] E. StrÖm, Y. Cao, Y.M. Yao, Trans. Nonferrous Met. Soc. China 17 (2007) 1282–1286.
[8] Y.L. Zhang, H.J. Li, Q.G. Fu, X.Y. Yao, K.Z. Li, G.S. Jiao, Carbon 46 (2008) 179–182.
[9] T.C. Lu, A.G. Evans, R.J. Hecht, R. Mehrabian, Acta Metall. Mater. 39 (1991) 1853–1862.
[10] B.K. Yen, T. Aizawa, J. Kihara, J. Am. Ceram. Soc. 79 (1996) 2221–2225.
[11] Y.J. Qiao, H.X. Zhang, C.Q. Hong, X.H. Zhang, J. Phys. D: Appl. Phys. 42 (2009) 105413.
[12] J. Xu, Y. Wang, S.Y. Jiang, Nanoscale 2 (2010) 394.
[13] M.D. Segall, J.D. Philip, M.J. Lindan, C.J. Probert, P.J. Pickard, S.J. Hasnip, M.C. Clark, Payne, J. Phys., Condens. Matter 14 (2002) 2717–2744.
[14] A.E. Mattsson, P.A. Schultz, M.P. Desjarlais, T.R. Mattsson, K. Leung, Model Simul. Mater. Sci. Eng. 13 (2005) R1–R31.
[15] L.Z. Cao, J. Shen, N.X. Chen, J. Alloys Comp. 336 (2002) 18–28.
[16] J.P. Perdew, K. Burke, M. Ernzerhof, Phys. Rev. Lett. 77 (1996) 3865–3868.
[17] H.J. Monkhorst, J.D. Pack, Phys. Rev. B 16 (1977) 1748–1749.
[18] T.H. Fischer, J. Almlof, J. Phys. Chem. 96 (1992) 9768–9774.
[19] R. Hill, Proc. Phys. Soc. A 65 (1952) 349–354.
[20] J. Haines, J.M. Léger, G. Bocquillon, Annu. Rev. Mater. Res. 31 (2001) 1–23.
[21] D.M. Teter, R.J. Hemley, Science 271 (1996) 53–55.
[22] S.F. Pugh, Philos. Mag. 45 (1954) 823–826.
[23] W. Koster, H. Franz, Metall. Rev. 6 (1961) 1–56.
[24] K. Tanaka, K. Nawata, H. Inui, M. Yamaguchi, M. Koiwa, Intermetallics 6 (1998) 607–611.
[25] I.N. Frantsevich, F.F. Voronov, S.A. Bokuta, Elastic Constants and Elastic Moduli of Metals and Insulators Handbook, Naukova Dumka, Kiev, 1983. pp. 60–180.
[26] P.S. Frankwicz, J.H. Perepezko, Mater. Sci. Eng. A 246 (1998) 199–206.
[27] E. Chi, J. Shim, J. Kwak, H. Balk, J. Mater. Sci. 31 (1996) 3567–3572.
[28] S. Zhang, H. Xie, X. Zeng, P. Hing, Surf. Coat. Technol. 122 (1999) 219–224.
[29] C.T. Chuang, C.K. Chao, R.C. Chang, K.Y. Chu, J. Mater. Process. Technol. 201 (2008) 770–774.
[30] A. Mani, P. Aubert, F. Mercier, H. Khodja, C. Berthier, P. Houdy, Surf. Coat. Technol. 194 (2005) 190–195.
[31] K. Niihara, Ceramics 20 (1985) 1218–1224.
[32] J.J. Kim, Y. Choi, S. Suresh, A.S. Argon, Science 295 (2002) 654–657.

[33] G. Bolelli, V. Cannillo, L. Lusvarghi, F.P. Mantini, E. Gualtieri, C. Menozzi, Mater. Lett. 62 (2008) 1557–1560.
[34] J. Schiøtz, K.W. Jacobsen, Science 301 (2003) 1357–1359.
[35] M.W. Chen, E. Ma, K.J. Hemker, H.W. Sheng, Y.M. Wang, X.M. Cheng, Science 300 (2003) 1275–1277.
[36] Y. Gan, B.L. Zhou, Scripta Mater. 45 (2001) 625–630.
[37] G.P. Zhang, Y. Liu, W. Wang, J. Tan, Appl. Phys. Lett. 88 (2006) 013105.
[38] G. He, J. Eckert, W. Loeser, L. Schultz, Nature Mater. 2 (2003) 33–37.
[39] L. Lu, M.L. Sui, K. Lu, Science 287 (2000) 1463–1465.
[40] Y.M. Wang, M. Chen, F. Zhou, E. Ma, Nature 419 (2002) 912–915.
[41] C.C. Hays, C.P. Kim, W.L. Johnson, Phys. Rev. Lett. 84 (2000) 2901–2904.
[42] Y.H. Liu, G. Wang, R.J. Wang, D.Q. Zhao, M.X. Pan, W.H. Wang, Science 315 (2007) 1385–1388.
[43] K. Holmberg, H. Ronkainen, A. Laukkanen, K. Wallin, S. Hogmark, S. Jacobson, U. Wiklund, R.M. Souza, Per Ståhle, Wear 267 (2009) 2142–2156.
[44] P.B. Kadolkar, T.R. Watkins, J.Th.M. De Hosson, B.J. Kooi, N.B. Dahotre, Acta Mater. 55 (2007) 1203–1214.